# Plug-in Hybrid Electric Vehicle Charge Pattern Optimization for Energy Cost and Battery Longevity

Saeid Bashash, Scott J. Moura, Joel C. Forman, and Hosam K. Fathy[*]

Control Optimization Laboratory, Department of Mechanical Engineering,

The University of Michigan, Ann Arbor, MI 48109, USA.

**Abstract**

This paper examines the problem of optimizing the *charge pattern* of a plug-in hybrid electric vehicle (PHEV), defined as the timing and rate with which the PHEV obtains electricity from the power grid. The optimization goal is to simultaneously minimize *(i)* the total cost of fuel and electricity and *(ii)* the total battery health degradation over a 24-hour naturalistic drive cycle. The first objective is calculated for a previously-developed stochastic optimal PHEV power management strategy, whereas the second objective is evaluated through an electrochemistry-based model of anode-side resistive film formation in lithium-ion batteries. The paper shows that these two objectives are conflicting, and trades them off using a non-dominated sorting genetic algorithm. As a result, a Pareto front of optimal charge patterns is obtained. The effects of electricity price and trip schedule on the optimal Pareto points and the PHEV charge patterns are analyzed and discussed.

**Keywords:** Plug-in hybrid electric vehicles; Charge pattern optimization; Lithium-ion battery degradation.

---

[*] Corresponding author. Phone: +1 (734) 330 5008. E-mail address: hfathy@umich.edu.

## 1- Introduction

This paper examines *plug-in hybrid electric vehicles (PHEVs)*, defined as vehicles that can use both fuel and electricity for propulsion, and can obtain the latter either through onboard generation or by plugging into the grid. The paper's overarching goal is to optimize the *charge pattern* of such PHEVs, defined as the timing and rate with which they obtain electric energy from the grid. We perform this optimization with two objectives in mind, namely, *(i)* minimizing the overall cost of daily PHEV energy consumption, and *(ii)* minimizing the concurrent damage to PHEV batteries. Such optimization is an important step towards achieving the potential economic and environmental benefits of PHEVs envisioned by the scientific community [1-5].

The literature has examined PHEV charge patterns from a number of different perspectives. The most commonly studied charge pattern is overnight charging, where PHEVs start charging late at night, e.g., 10p.m. or midnight [4-6]. Evening charging is another scenario which has also been examined [5]. More sophisticated trip- and price-dependent strategies such as "immediate end of travel" charging, "optimized to off-peak" charging, and "opportunity charging" have also been assumed and used for the prediction of total PHEV load [6]. This paper optimizes PHEV charging in a way that takes into account, for the first time, the combined effects of total energy cost, battery health, electricity pricing, and PHEV driving patterns. The charge patterns obtained through this optimization are substantially different from those optimized for energy cost or battery health alone.


One of the key contributors to total PHEV acquisition cost is battery storage capacity, which tends to degrade with time and cycling [7-9]. This paper focuses specifically on PHEVs that

employ lithium-ion batteries for energy storage. The literature provides two distinct types of Li-ion battery models: *(i)* empirical models that are built on experimental measurements of battery input-output behavior, such as equivalent circuit models [10, 11], and *(ii)* higher-fidelity models derived from the principles of battery electrochemistry [12, 13]. The modeling of capacity fade and life degradation has been more extensively pursued under the second category. This paper adopts a first-principles electrochemistry-based battery model developed by Doyle *et al.* [12] and Fuller *et al.* [13], and later expanded by Ramadass *et al.* [14] through the addition of a capacity fade component. In this model, the primary mechanism for battery degradation is an assumed side reaction within the negative electrode (anode), which causes the irreversible growth of a solid electrolyte interface (SEI) layer on the electrode, and the loss of cyclable lithium ions. Although there are several other degradation mechanisms affecting Li-ion batteries, such as overheating, overcharging, deep discharging, etc. [15], in this paper we only minimize SEI film growth as a key cause of battery degradation. In doing so, we develop a generalizable PHEV charge pattern optimization method that can be used for minimizing degradation through other mechanisms as well.

To the best of the authors' knowledge, there are currently no published articles in the PHEV literature that optimize the charge pattern of a PHEV for both energy cost and battery health. Thus, this paper is the first to analyze this problem. Since we deal with optimizing two objectives which are conflicting (as will be explained in the paper), we use a multiobjective optimization algorithm, namely, the non-dominating sorting genetic algorithm II (NSGA-II) developed by Deb *et al.* [16]. Our goal is to obtain an optimal Pareto front that trades off these two objectives. To quantify the total daily energy cost, we use a mid-size sedan PHEV model with a previously-developed optimal on-road power management strategy [17, 18], and a

naturalistic 24-hour drive cycle with two (morning and afternoon) half-trips. Moreover, the measure of battery degradation is obtained through a reduced-order representation of the electrochemistry-based battery model discussed above. To account for daily variations in electricity prices, we use the pricing policy of the DTE Energy Company for electric vehicles in the State of Michigan [19]. Putting all of these elements together, we finally optimize the PHEV charge pattern, and study various solutions from the resulting Pareto front.

The remainder of the paper is organized as follows: Section 2 provides a brief review of the PHEV model and its optimal on-road power management. Section 3 reviews the abovementioned high-fidelity Li-ion battery model and its life degradation component. Section 4 then formulates the charge pattern optimization problem for PHEVs. Section 5 presents and discusses the optimal PHEV charge patterns. Finally, Section 6 summarizes the paper's main conclusions.

## 2- PHEV Model and Optimal Power Management

The two objectives optimized in this paper, namely, energy cost and battery health, depend not only on PHEV charging, but also on how the given PHEV operates on the road. Therefore, modeling PHEV on-road power management is an important prerequisite to charge pattern optimization. On-road power management can be optimized using a number of different methods, including deterministic dynamic programming (DDP) when the drive cycle is known [20, 21], and stochastic dynamic programming (SDP) when a statistical drive cycle description is available [17, 18]. This paper adopts a PHEV model used by the authors in a previous study [17] as well as the on-road power management algorithm optimized for that PHEV using SDP. We describe both briefly below.

*2.1. PHEV Model*

The PHEV model examined in this paper is based on a power-split mid-size sedan, similar in configuration, dynamics, and design to the 2002 Toyota Prius, but with an 8 kWh Li-ion battery pack. The supervisory power management algorithm, which determines the optimal split of engine and battery power, is developed using SDP techniques. We summarize the PHEV model and associated optimal supervisory control strategy here for comprehensiveness, but readers are encouraged to study [17, 18] for more details.
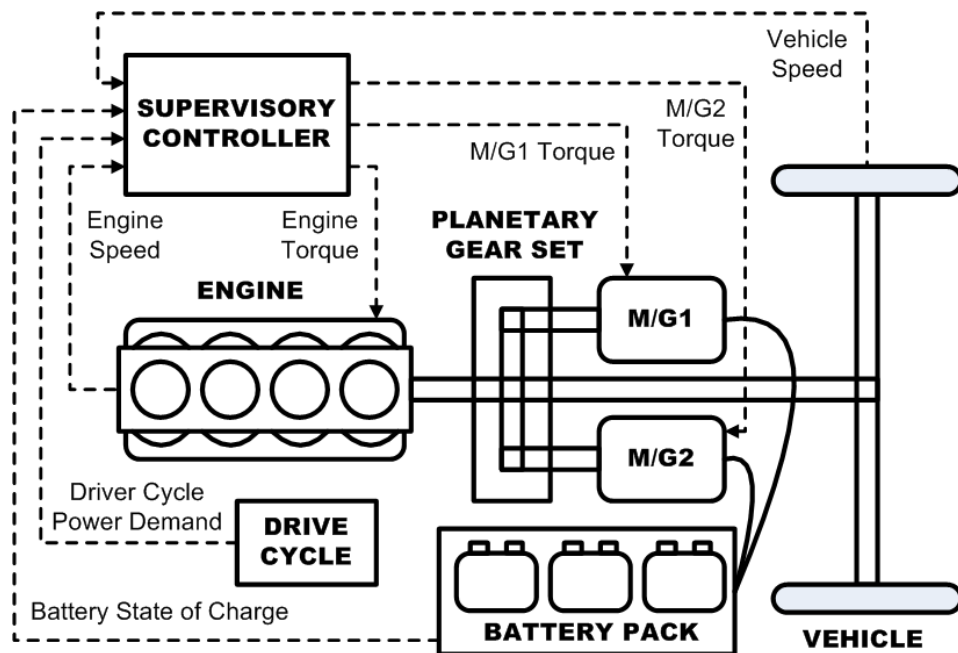


Figure 1. PHEV model components, supervisory controller, and signal flow. Note that the signal flow forms a state feedback control architecture.

Figure 1 presents a conceptual map of the key interactions between the PHEV, the drive cycle, and the supervisory power management algorithm. The supervisory power management algorithm attempts to meet drive cycle power demand by adjusting three control inputs: engine torque, electric motor/generator 1 (M/G1) torque, and M/G2 torque. These inputs are determined

by a nonlinear static feedback law, which depends functionally on the PHEV model states: engine speed, vehicle velocity, battery pack SOC, and drive cycle power demand. The first three states are governed by PHEV dynamics, while power demand is governed by a Markov chain which captures drive cycle dynamics, described in further detail below.

## 2.1.1. Mechanical Subsystem

The planetary gearset is at the heart of the power-split configuration. This three-port device couples the engine, M/G1, and M/G2 crankshafts. The dynamic-algebraic equations that describe this device are governed by Euler's law and a kinematic constraint relating component speeds:

$$\begin{bmatrix} I_e & 0 & 0 & R+S \\ 0 & I_{M/G1} & 0 & -S \\ 0 & 0 & I'_{M/G2} & -R \\ R+S & -S & -R & 0 \end{bmatrix} \begin{bmatrix} \dot{\omega}_e \\ \dot{\omega}_{M/G1} \\ \dot{\omega}_{M/G2} \\ F \end{bmatrix} = \begin{bmatrix} T_e \\ T_{M/G1} \\ T'_{M/G2} \\ 0 \end{bmatrix} \tag{1}$$

The terms $I'_{M/G2}$ and $T'_{M/G2}$ are effective inertia and torques

$$I'_{M/G2} = I_{M/G2} + (I_w + mR_{tire}^2)/K^2 \tag{2}$$

$$T'_{M/G2} = T_{M/G2} + F_{road}R_{tire}/K \tag{3}$$

$$F_{road} = 0.5\rho C_d A_{fr} v^2 + \mu_{roll} mg \tag{4}$$

where $F_{road}$ includes viscous aerodynamic drag and rolling friction forces.

Through algebraic manipulations one may analytically solve for the state variables without explicitly determining the gear force $F$ or inverting the matrix on the LHS of (1). This process results in two degrees of freedom, since there exist three ordinary differential equations and one algebraic constraint. Hence, the control inputs include engine torque $T_e$ and $T_{M/G1}$ M/G1 torque.

## 2.1.2. Electric Subsystem

To solve the supervisory power management control problem, the battery pack is modeled by an equivalent circuit. This simplified system includes an open circuit voltage in series with an internal resistance, both of which are parametric functions of battery SOC. Both M/G1 and M/G2 interface with the battery pack, as shown in Fig. 1. These devices are modeled by power efficiency maps supplied by ADVISOR 2004 [22]. The electrical powertrain also consists of power electronics, whose dynamics are fast enough to be modeled as instantaneous. Hence, the governing equations for the electric subsystem are given by:

$$S\dot{O}C = -\frac{V_{oc} - \sqrt{V_{oc}^2 - 4P_{batt}R_{batt}}}{2Q_{batt}R_{batt}} \tag{5}$$

$$P_{batt} = T_{M/G1}\omega_{M/G1}\eta_{M/G1}^{k_{M/G1}} + T_{M/G2}\omega_{M/G2}\eta_{M/G2}^{k_{M/G2}} \tag{6}$$

$$k_i = \begin{cases} -1, & T_i\omega_i > 0 \\ 1, & T_i\omega_i \leq 0 \end{cases} \text{ for } i = \{M/G1, M/G2\} \tag{7}$$

We compute the electric current flow through the battery pack according to $I = S\dot{O}CQ_{batt}$, which provides the input signal used for simulating the high-fidelity battery model, described in Section 3, for the charge pattern optimization problem.

## 2.1.3. Drive Cycle Model

A stochastic model of drive cycle behavior is utilized to solve the supervisory power management algorithm. This formulation results in a power management algorithm that is optimal with respect to a statistical description of driving schedules, as opposed to a single drive cycle. Mathematically, the stochastic drive cycle model is given by the following Markov chain

$$p_{ijm} = \Pr(P_{dem}(k+1) = j | P_{dem}(k) = i, v(k) = m) \tag{8}$$

which maps power demand-velocity pairs to a probability distribution over power demand in the next time step. These transition probabilities are identified from certification cycles and real-world micro-trip data [22].

2.1.4. Optimal Power Management Problem Formulation

The objective of the supervisory on-road power management algorithm is to minimize the expected consumption cost of both fuel (from the gas pump) and electricity (from the grid) over a stochastic distribution of drive cycles. Mathematically, this is written as a discounted infinite-horizon problem, where $k$ is the discrete-time variable:

$$\text{Minimize: } J = \lim_{N \to \infty} E_{P_{dem}}\left[\sum_{k=0}^{N-1} \gamma^k g\big(x(k), u(k)\big)\right] \tag{9}$$

$$\text{Subject to: } \begin{array}{l} x(k+1) = f(x(k), u(k)) \\ x \in X \\ u \in U(x) \end{array} \tag{10}$$

The cost function $g(x(k), u(k))$ represents the instantaneous cost of fuel consumption and grid-provided electricity. The fuel and electricity prices are set to 3.44 USD/gallon and 0.08 USD/kWh, respectively, which are representative of the 2008 national averages in the USA. The optimization is also subject to the PHEV model dynamics , limits on the PHEV state and control signals, and a power conservation constraint that ensures the power sources continuously meet drive cycle power demand, as described in (9). The result is that the supervisory control algorithm carefully blends engine and battery power when the battery pack SOC is greater than 25% (the minimum allowable SOC). As the battery pack SOC approaches 25%, the algorithm enters a charge sustenance mode that maintains the SOC above 25% by operating similar to a conventional HEV. That is, the vehicle depletes battery energy when it is advantageous (low speeds and power demands), but regenerates SOC during other periods to maintain a relatively

constant charge level. It is important to note that the supervisory on-road power management algorithm is explicitly designed to minimize an average energy consumption cost, but does not take into account factors that cause battery pack degradation. These two factors, energy consumption cost and battery pack aging, are the subject of the remainder of this paper.
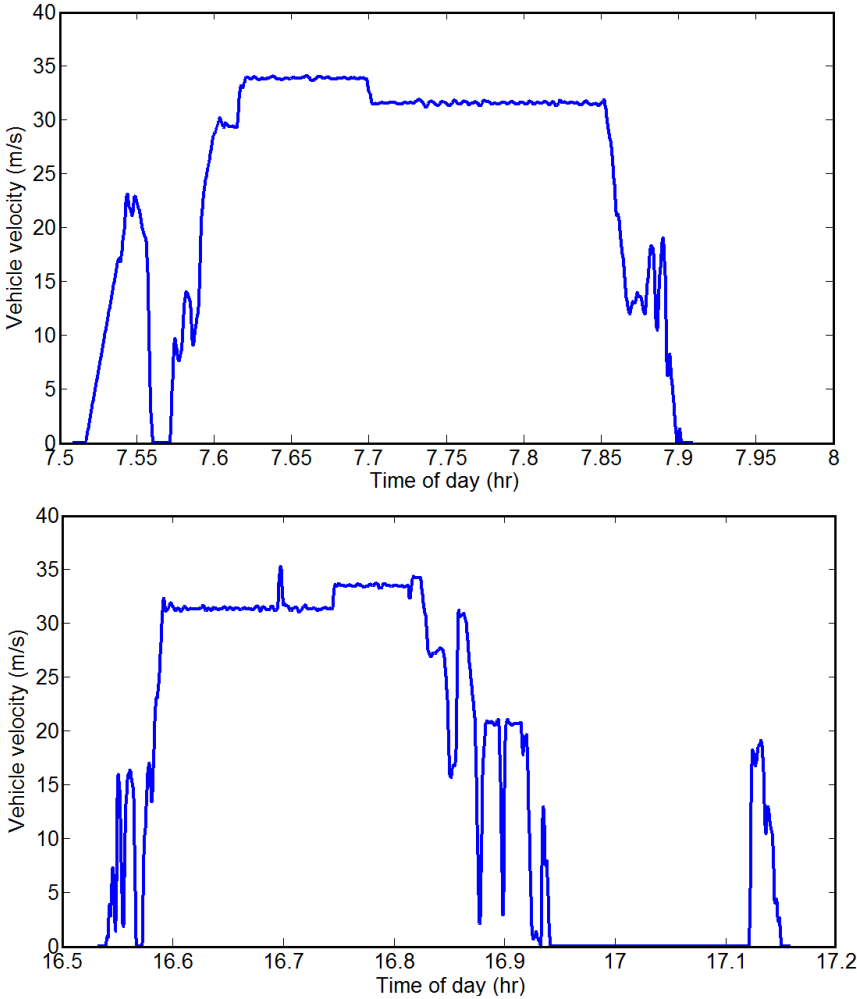


Figure 2. A sample suburban naturalistic drive cycle with two half trips, one in the morning and one in the afternoon (vehicle velocity is zero during the rest of the day).

## 2.2. Simulations of PHEV with Optimal Power Management

Figure 2 depicts a sample 24-hour suburban naturalistic drive cycle with two active parts. This drive cycle will be used throughout the paper for simulating the PHEV model. Here, we

examine the effects of the initial battery SOC on the final energy costs when the PHEV follows the drive cycle.
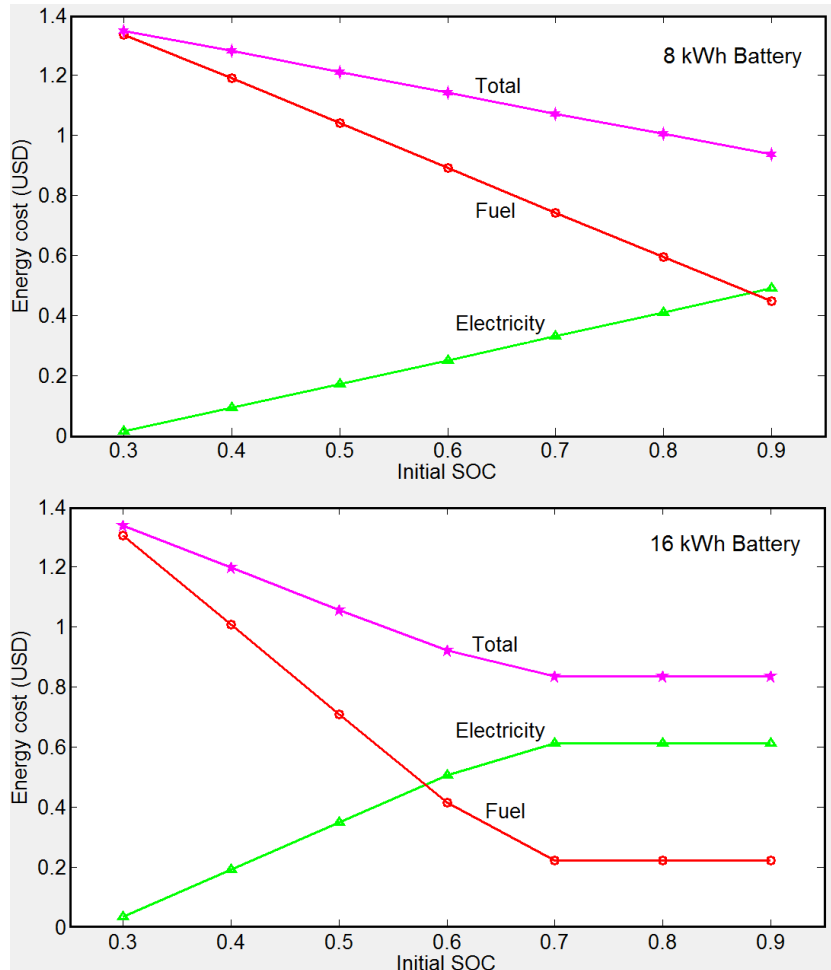


Figure 3. Energy costs versus initial battery SOC for the optimal power management strategy with two different battery sizes: an 8 kWh (top) and a 16 kWh battery (bottom).

Figure 3 depicts the simulation results for only the first part of the drive cycle (similar results are obtained for the second part). Two battery sizes are considered: an 8 kWh and a 16 kWh battery pack. For the smaller battery, as the initial battery SOC increases, the cost of electricity over the course of the half-trip increases as well, but the fuel and the total energy costs decrease. This is due to the fact that electricity allows less expensive propulsion than fuel. For the 16 kWh

battery, a similar trend is obtained, but only up to a certain initial SOC (about 70% in this case). Further increase of the initial SOC does not reduce the energy costs anymore, because the initial battery charge exceeds the amount needed for the trip. Hence, we can conclude that t*he higher the initial battery SOC before a given trip, the smaller the total energy cost at the end of that trip, assuming that the trip consumes all the stored electricity.* Note that this trend may change if the electricity price substantially increases compared to the fuel price.

Now that the effects of the initial battery SOC on the energy costs are examined, we examine, next, the effects of initial battery SOC on battery health degradation through an electrochemistry-based Li-ion battery model.

**3- High-fidelity Li-ion Battery Model**

This section summarizes the model used in this paper for predicting the cycling performance and SEI layer growth in a lithium-ion battery. The model is pseudo-two dimensional, and includes degradation effects [14, 23], where the main cause of degradation is assumed to be an irreversible side reaction in the anode. As a result of this side reaction, a resistive film builds up in the anode which increases the internal resistance of the battery and leads to capacity loss and self discharge. Simpler models have been used to monitor battery state of charge and state of health [24-27]. However, these models have been developed to only observe battery degradation effects, not to predict them. The model we consider herein is attractive because it can both capture battery health degradation effects and simulate battery dynamics over a very wide range of cycles (due to its predictive, 1st principles nature). The following subsections present a brief overview of both this model [12-14] as well as efforts to reduce its computational complexity [28-31] and validate it against experimental data.

## 3.1. Battery Model Review

Lithium ion batteries store electric energy by shuffling lithium ions between low and high potential energy states via a set of electrochemical processes. Lithium ions have the lowest energy when they are in the positive electrode (cathode) and the highest energy when they are in the negative electrode (anode). During charging, external current forces lithium ions to move from the cathode to the anode. During discharge, ions naturally move from the anode to the cathode, creating a useful current. Lithium ions movement is governed by two diffusion processes, as well as two electrochemical reactions driven by overpotentials. These electrochemical reactions allow the lithium ions to transfer between solid and solution phases via intercalation currents.

Based on the model developed by Doyle *et al.* and Fuller *et al.* [12, 13], and expanded by Ramadass *et al.* [14], the governing equations of solid phase and solution phase potentials (represented by $\phi_1$ and $\phi_2$, respectively) are given by Ohm's law as follows[†]:

$$\nabla \cdot \left( \sigma_j^{eff} \nabla \phi_{1,j} \right) - J = 0, \; j = n, p \tag{11}$$

$$\nabla \cdot \left( \kappa^{eff} \nabla \phi_2 \right) + \nabla \cdot \left( \kappa_D \nabla \ln \left( c_2 \right) \right) + J = 0 \tag{12}$$

where $\sigma_j^{eff}$ is the effective conductivity of electrode *j* (where *n* stands for the negative electrode and *p* for the positive electrode); $\kappa^{eff}$ and $\kappa_D$ represent the concentration-dependent effective and diffusional conductivities of the solution phase; $J = J_1 + J_{sd}$ is the total intercalation current density calculated from the Butler-Volmer expression for the main intercalation reaction current density given by:

---

[†] Lists of all parameter values and the boundary conditions for the partial differential equations, i.e., Eqs. (11), (12), (18) and (19), can be found in Ref. [31].

$$J_1 = a_j i_{0,j} \left[ \exp\left( \frac{\alpha_{a,j} F}{RT} \eta_j \right) - \exp\left( -\frac{\alpha_{c,j} F}{RT} \eta_j \right) \right], \quad j = n, p \tag{13}$$

where

$$i_{0,j} = k_j \left( c_{1,j}^{\max} - c_{1,j}^S \right)^{\alpha_{a,j}} \left( c_{1,j}^S \right)^{\alpha_{c,j}} \left( c_2 \right)^{\alpha_{a,j}}, \quad j = n, p \tag{14}$$

and a side intercalation reaction current density governed by:

$$J_{sd} = -i_{0,sd} a_n \exp\left( -\frac{\alpha_{c,n} F}{RT} \eta_{sd} \right) \tag{15}$$

In these equations, $a$ and $k$ are the specific area of the porous electrode and the rate constant of electrochemical reaction, respectively; $\alpha_a$ and $\alpha_c$ are the anodic and cathodic transfer coefficients of the electrochemical reaction; $F$, $R$, and $T$ respectively denote the Faraday's constant, universal gas constant and the temperature; $c_1$ and $c_1^{\max}$ represent the lithium concentration in the solid phase, and its maximum limit; $i_0$ and $i_{0,sd}$ are the exchange current densities for the main and the side reactions, respectively, and $\eta$ and $\eta_{sd}$ are the corresponding overpotentials, given by:

$$\eta_j = \phi_1 - \phi_2 - U_{ref,j} - \frac{J}{a_n} R_{film}, \quad j = n, p \tag{16}$$

$$\eta_{sd} = \phi_1 - \phi_2 - U_{ref,sd} - \frac{J}{a_n} R_{film} \tag{17}$$

where $U_{ref,j}$ is the SOC-dependent local equilibrium potential of the main reaction, $R_{film}$ is the side film resistance in anode, and $U_{ref,sd}$ is the equilibrium potential for the side reaction.

In the solution phase, lithium ions are governed by a diffusion law combined with an intercalation current density term transferring ions between the solution and the solid:

$$\varepsilon_2 \frac{\partial c_2}{\partial t} = \nabla \cdot \left( D_2^{eff} \nabla c_2 \right) + \frac{1-t^+}{F} J \tag{18}$$

where $\varepsilon_2$ represents the volume fraction of the solution phase, $D_2^{eff}$ denotes the effective diffusion coefficient of lithium in the solution phase, and $t^+$ stands for the transference number.

The solid phase concentration is governed by a radially symmetric spherical diffusion:

$$\frac{\partial c_{1,j}}{\partial t} = \frac{D_{1,j}}{r^2} \frac{\partial}{\partial r} \left( r^2 \frac{\partial c_{1,j}}{\partial r} \right) \tag{19}$$

where $D_1$ is the diffusion coefficient of lithium in the solid phase, and $r$ is the sphere radius. This solid diffusion process occurs at every point in anode and cathode, and is connected to the solution via the intercalation current density.

Finally, a resistive film builds up in anode as a result of side reaction:

$$\frac{\partial \delta_{film}}{\partial t} = -\frac{J_{sd} M_p}{a_n \rho_p F} \tag{20}$$

with $\delta_{film}$ being the thickness of the resistive film, and $M_p$ and $\rho_p$ representing the molecular weight and density of the side reaction product, respectively. This results in the resistance increase of the side film as follows:

$$R_{film} = R_{SEI} + \frac{\delta_{film}}{K_p} \tag{21}$$

where $R_{SEI}$ denotes the initial solid/electrolyte interface resistance, and $K_p$ represents the conductivity of the side reaction product, respectively. The growth of the resistive film corresponds to the loss of cyclable lithium ions and therefore battery capacity fade.

Before moving to the next section, i.e. battery model reduction, it is important to remark that in the simulations of the battery model in this paper *battery voltage* corresponds to the solid phase potential at the rightmost point of the cathode (right collector); *SOC* represents the spatial average of lithium ions concentration in the anode divided by its maximum value, and the *resistive film growth rate* corresponds to its the spatial average in the anode.


### 3.2. Battery Model Reduction

Equations (11)-(21) form a set of differential algebraic equations that must be solved numerically to simulate the battery model. There are two major numerical difficulties associated with this model: (*i*) the existence of a large number of state variables (reasonable discretizations of the model's partial differential equations can easily yield several thousands of state variables), and (*ii*) the presence of a large set of nonlinear algebraic constrains, i.e., equations (11)-(17), that must be solved at every point along the electrodes in every instant of time. These equations control the intercalation current and potentials at each point within the electrodes.

Due to the model's large dimension, several model reduction methods have been proposed in the literature to improve its computational efficiency [28-31]. This paper improves the model's computational speed by adopting a model reduction approach proposed in previous work by the authors [31]. In this approach, a quasi-linearization strategy is adopted for the nonlinear algebraic constraints, and a family of analytic Padé approximations is used to reduce the number of state variables associated with the spherical diffusion process. The main advantage of the approach is that it maintains the fidelity of the model within a frequency range of interest, making it suitable for effective on-road PHEV discharge simulation, which often includes both

high-frequency and low-frequency components. Interested readers are encouraged to study [31] for more details of the approach.

Reducing the battery model's computational complexity makes it possible to identify its parameters based on experimental cycling data. The following section describes an experimental setup used to examine the SOC dynamics of sample battery cells, and the results of fitting the above model to these SOC dynamics.

### 3.3. Experimental Setup and Parameter Identification of High-Fidelity Battery Model

A custom-built battery test system, shown in Fig. 4, has been developed to identify and validate the high-fidelity battery model described in Section 3.1. The system is hardware-in-the-loop capable via a dSPACE DS1104 R&D controller board. The charging and discharging power is provided, respectively, by a Sorenson DCS 50-20E programmable power supply and Sorenson SLH-60-120-1200 DC programmable electronic load. Sensor electronics have also been developed to record terminal voltage, current, and surface temperature of the battery cell canister. The batteries under examination are commercial 2.3 Ah 3.3V nominal voltage Li-ion cells containing LiFePO$_4$ cathode chemistries [A123] in a 26650 format. These cells are designed for high power operations, and are therefore well-suited for PHEV applications.

With this setup, we run a series of constant current, constant voltage (CC-CV) "chirp" cycles to obtain data used for offline parameter identification. Specifically, these load profiles cycle between 2.6V and 3.6V, for current rates of 5C, 2.5C, 1C, 0.75C, and 0.25C[‡]. These input profiles contains a wide range of frequency content, which is important for identifying

---

[‡] C-rate is a standard unit for battery charge and discharge, representing the ratio of the applied current (in Amp) to the rated capacity of battery (in Amp-hour). For instance, at the charge rate of $1C$ the battery can be fully charged in one hour, whereas at $2C$ it only takes half hour to charge the battery for a full SOC range.

parameters ranging from the equilibrium potentials to diffusion coefficients. Moreover, the use of these profiles is also commensurate with the frequency content that high-power/energy batteries typically experience in PHEV applications.
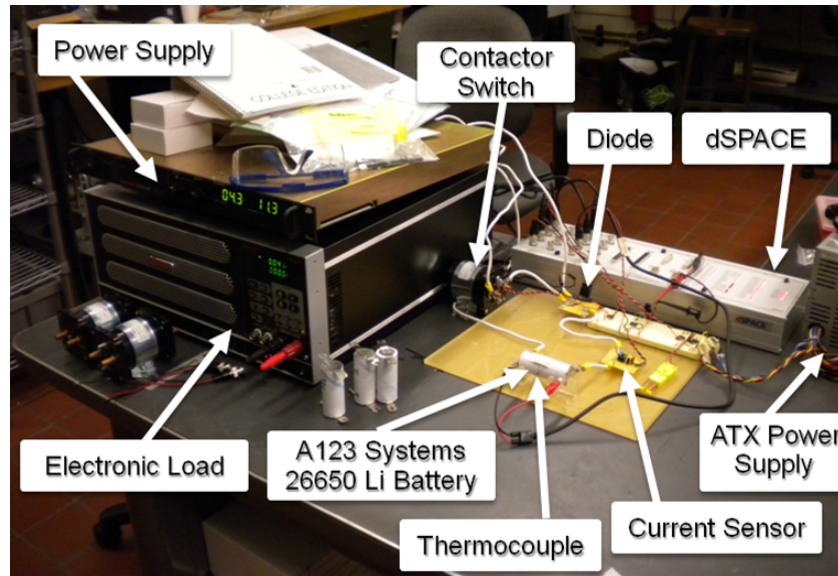


Figure 4. Custom-built experimental battery test system used for parameter identification and validation of the high-fidelity battery model.

Figure 5 depicts the described chirp current profile applied to the battery cell and the corresponding voltage trajectory. The simulated response of the battery model to this current profile is plotted against the experimental voltage response for comparison. We fitted this simulated response to experimental data using a genetic optimizer that adjusted the entire parameter set of the battery model, except for the degradation sub-model parameters (these will be addressed in the following subsection). The optimizer attempts to minimize the error between the voltage response of the actual battery cell and the voltage response of the high-fidelity battery model for the given chirp cycle. Optimization is only performed over part of the chirp cycle, and the remainder of the cycle is used solely for validation. We can see a good agreement

being achieved between the model and the experiment through this optimization process. However, it should be remarked that these battery optimization efforts are ongoing, and will be discussed further in a future publication.
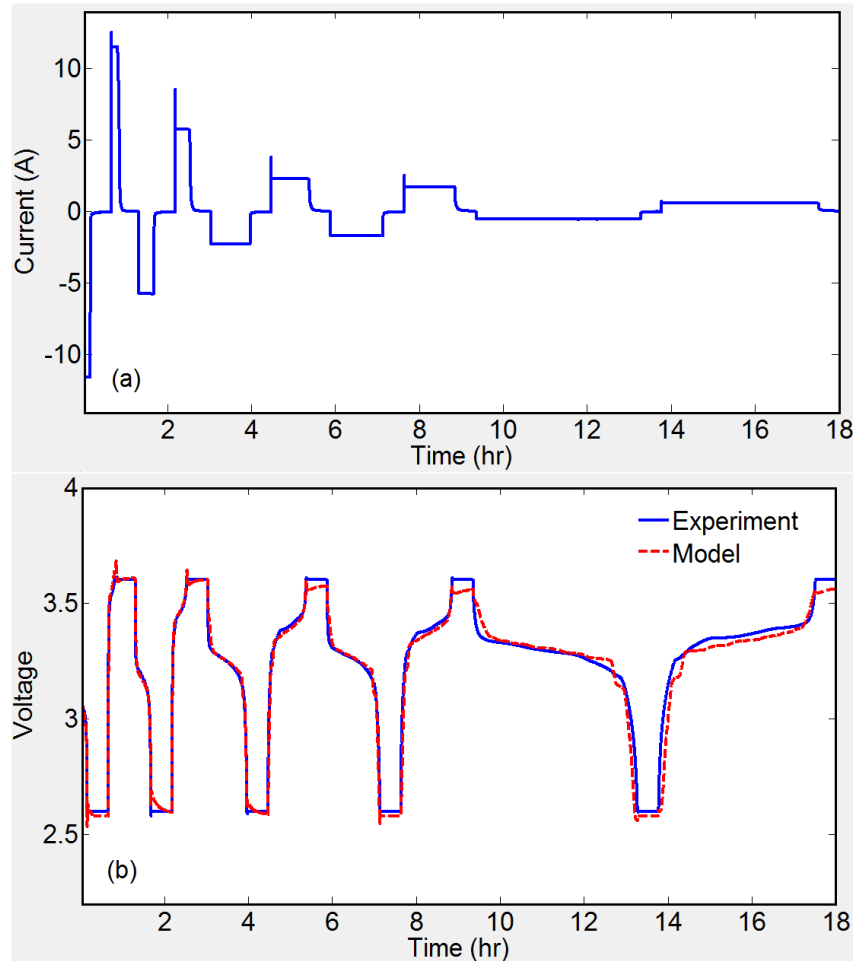


Figure 5. Experimental battery parameter identification results: (a) Applied current profile, and (b) Experimental and model voltage responses.
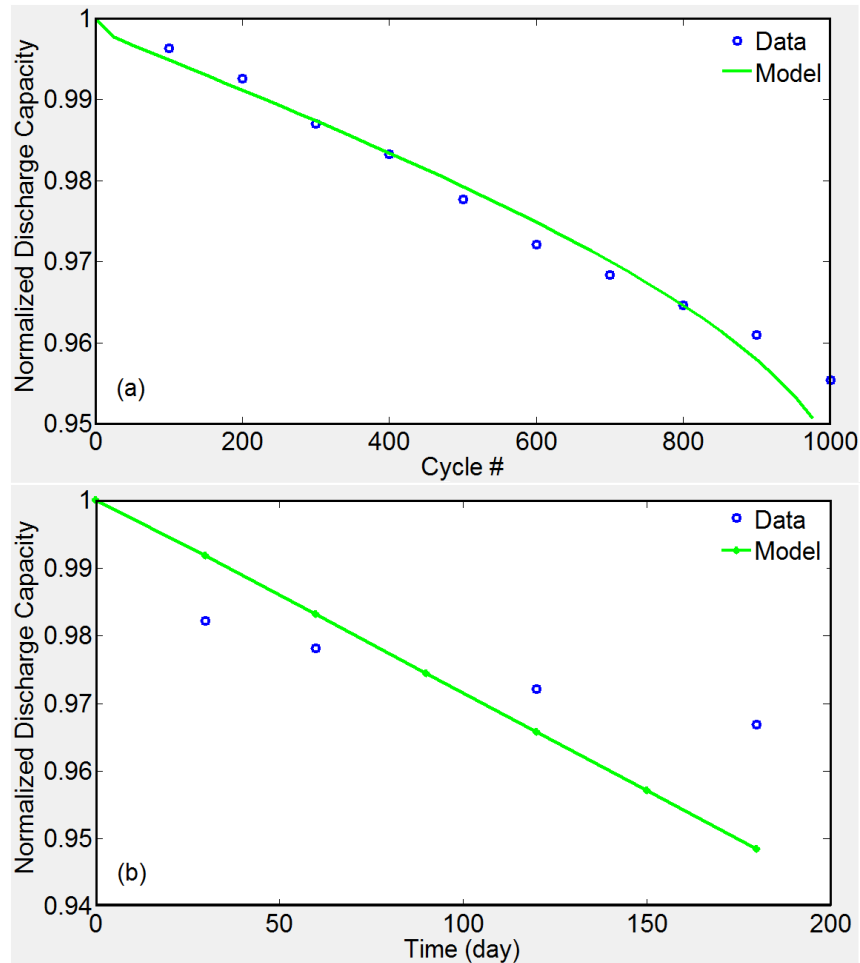
### 3.4. Battery Degradation Analysis

The previous subsection validated the SOC dynamics of the electrochemistry-based battery model against short-term experimental battery cycling data. This subsection examines the degradation component of the battery model using longer-term Li-ion battery degradation test

results. Optimization of the degradation component's parameters to experimental data is ongoing, and will be the focus of a future publication. This paper examines a representative set of degradation parameters, manually tuned to fit experimental battery degradation trends in both cycling and storage modes, assuming that the anode-side resistive film formation process responsible for battery degradation is active in both modes. The experimental degradation trends used in this section are obtained from the battery manufacturer's electronic resources and publications [32, 33].

Figure 6(a) compares the model's degradation response versus experimental manufacturer data [32] for a full CC-CV charge/discharge cycling test lasting 1000 cycles at room temperature, i.e. 25 $^\circ$ C. Furthermore, Figure 6(b) compares the model's degradation response to experimental manufacturer data [33] for storage at full charge over a time span of 6 months. The high-fidelity battery model matches the degradation measurements very well for the cycling case, and is also successful in capturing the degradation trend during storage. This justifies the use of the model for the charge pattern optimization study in this paper, especially considering the fact that the paper's methods are broadly applicable to other battery models that may capture the degradation trends below even better.

To further analyze the battery degradation characteristics, we simulate the battery model to obtain a useful map, qualitatively describing the battery degradation behavior. To obtain such a map, we first initialize the model at different SOC levels through initializing the concentration of lithium ions in the electrodes, and then apply input current at different rates to charge and discharge the battery. We monitor the *average* resistance growth rate in the anode at the first step of the simulation, and then plot it as a function of SOC and the charge rate.

Figures 6. Comparison between the battery model and the experimental manufacturer data in (a) CC-CV cycling and (b) full-charge storage modes.

Figure 7 depicts the obtained map for an SOC range of 10% to 90% and a charging rate of -2C to 2C, with negative sign indicating discharge. From the degradation map we can see that at the low and high SOC ends the battery tends to degrade faster, especially when it is subject to high-rate charging. Moreover, battery degradation takes place at a slower pace during charge depletion, compared to charging or storage. To examine battery capacity fade during energy storage, we plot a sub-trajectory of the map corresponding to zero charge rate, as shown in Figure 8. The sub-trajectory shows that battery degradation is faster at higher storage states of charge. Thus, energy storage at high SOCs can play a key role in battery degradation.
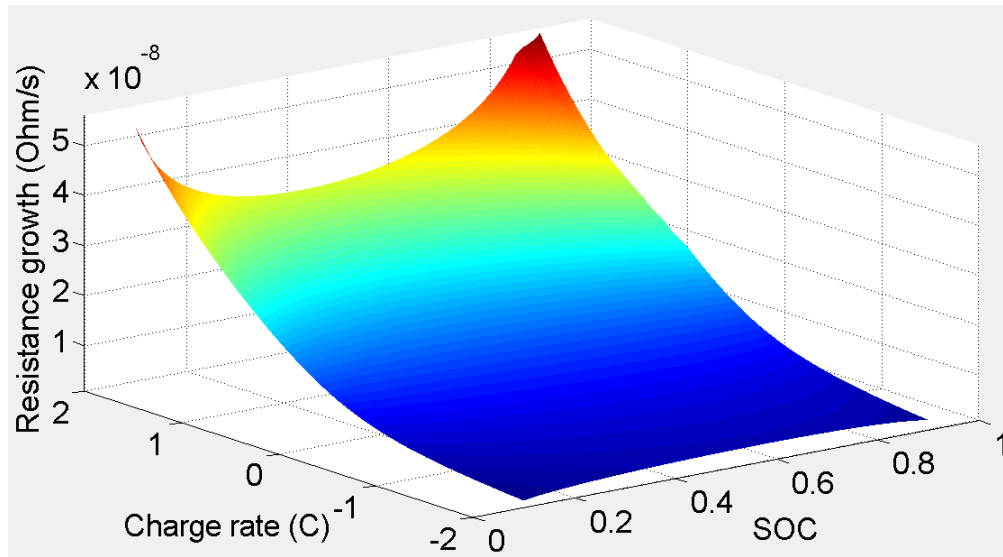
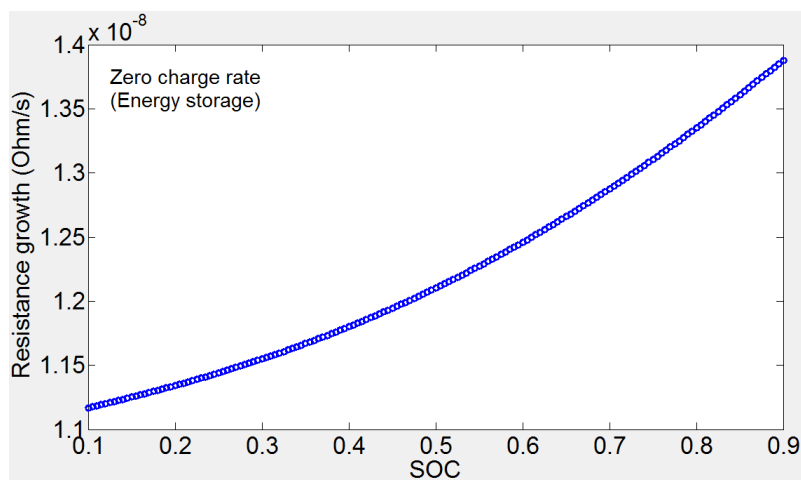Figure 7.  Battery degradation map.



Figure 8. Battery degradation response in energy storage.

In the next section, we will use the PHEV model together with the battery model in a multiobjective genetic optimization algorithm to obtain the optimal PHEV charge patterns.

**4- PHEV Charge Pattern Optimization**

This paper pursues two PHEV charge pattern optimization objectives.  One objective is to minimize the total energy cost for a PHEV over a given daily drive cycle, and the other objective

is to reduce the amount of resistive film buildup in the battery, and thus improve its longevity. We use the non-dominated sorting genetic algorithm II (NSGA-II) developed by Deb *et al.* [16] for this multiobjective optimization problem. Our use of NSGA-II makes it possible to obtain the entire Pareto front of optimal charge patterns in a single optimization run. This is beneficial not only from the computational standpoint, but also from the perspective of picturing and understanding the tradeoffs between energy cost and battery degradation.

*4.1. Optimization Procedure*

Figure 9 depicts the schematic diagram of the PHEV charge pattern optimization process. We have parameterized the problem such that the optimization variables are "the time", "the maximum amount", and "the rate" with which the PHEV receives charge before each trip. The "charge rate" is assigned as a mutual variable between all trips. During the charging phase, a CC-CV charging strategy is implemented on the battery model, based on the specified optimization variables. The electricity price consists of two different rates: during the on-peak hours (10.00 am to 7.00 pm) the electricity rate is 0.099 USD/kWh, while during the off-peak hours this rate reduces to 0.035 USD/kWh. This pricing profile is adopted from the DTE energy policy for electric vehicles in the State of Michigan, within the period of June to September 2009.

During the discharge phase, the vehicle model is initially simulated for the given drive cycle and the available battery charge. Then, the electric current signal absorbed by the electric drivetrain system during the trip is recorded and passed to the electrochemistry-based battery model to evaluate the extent of battery degradation while driving. During the dwelling intervals, battery degradation is evaluated from the battery model solely, at the stored SOC level. The total energy

cost and battery degradation at the end of the drive cycle are calculated by accumulating the separate pieces, and are then sent back to the optimizer to proceed to the next optimization step.
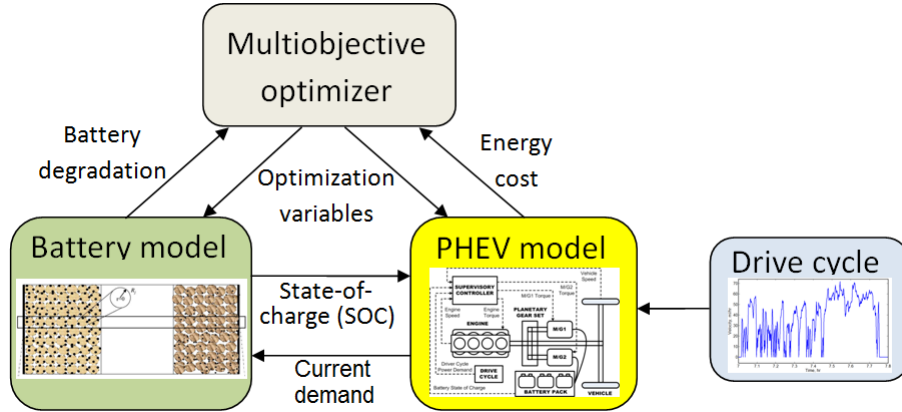


Figure 9. Schematic diagram of the PHEV charge pattern optimization process.

## 4.2. Optimization Formulation

For a drive cycle with $N$ separate trips the optimization objective is to:

$$\underset{x}{\text{Minimize}}\left\{\left(f_1(x) = \int_{24hr} J_{fuel}(x,t)dt + \int_{24hr} J_{elec}(x,t)dt\right) \& \left(f_2(x) = \bar{R}_{film}^{24hr}(x)\right)\right\}$$

$x = [x_1, x_2, x_3, ..., x_{2N+1}]$

$x_1$: Charge rate for all trips (between 0 and $1C$)　　　　　　　　　　　　　(22)

$x_{2i}, \ i = 1, 2, ..., N \ (i.e., x_2, x_4, ...x_{2N})$: Start time of charging for trip $i$

$x_{2i+1}, \ i = 1, 2, ..., N \ (i.e., x_3, x_5, ...x_{2N+1})$: Charge amount for trip $i$ (up to 90% SOC)

where $J_{fuel}$ and $J_{elec}$ are the instantaneous fuel and electricity dollar costs per unit time, $\bar{R}_{film}^{24hr}$ is the final resistance growth of the anode-side film at the end of the 24-hr simulation, and $x$ is the vector of optimization variables defining the charge patterns. The upper bound of battery SOC is set to 90% to avoid excessive degradation due to overcharging. The upper bound of charging rate is set to 1C which is within the approximate range of fast charging schemes envisioned for

PHEVs with average battery size. Finally, the upper and lower bounds of the variables associated with the charge times are set to cover the entire time span between the trips.

As stated earlier, this optimization problem deals with two conflicting objectives; while minimizing the total energy cost requires high SOC at the beginning of the trips, the battery tends to degrade faster at higher SOCs. Therefore, a single optimal point does not exist; instead, a family of optimal solutions in the form of a *Pareto front* can be obtained, as presented next.

**5- Optimal PHEV Charge Patterns**

In this section, we apply NSGA-II to the PHEV model to obtain its optimal charge patterns. According to the optimization formulation, Eq. (22), two independent optimization variables and one communal variable, i.e. the charging rate, are required for each active segment of a given drive cycle. Therefore, five optimization variables are required in total for the drive cycle studied in this paper.

*5.1. Optimal PHEV Pareto Front*

The result of PEHV charge pattern optimization are shown in Figure 10, where after 50 generations of a population of 80 members, a Pareto front of optimal solutions is formed. The total daily energy cost in the Pareto front ranges between $1.4 and $2.8 for the given drive cycle, while the added film resistance varies from 0.77 to 1.07 milliohms (per battery cell). To examine and compare the obtained optimal solutions, their added charge amount and charge rate are plotted in Figures 11 and 12, respectively.

Figure 11 demonstrates the total amount of added charge before the trips as well the portions of charge added before each trip. Because the PHEV battery cycles between 25-90% SOC range, the amount of added charge before each trip does not exceed 65%. From the figure, we see that the total amount of added charge increases as we move from the left to right end of the Pareto front, the direction along which the total energy cost decreases. Moreover, the added charge before the first trip dominates that before the second trip. That is, for a given amount of total daily charge, the portion of the charge added before the first trip is larger than that before the second trip, for the majority of the solutions. This trend is due to the fact that the first trip takes place during off-peak hours, whereas the second trip takes place during on-peak hours. Pulling the second charge time to the morning off-peak hours will result in further battery degradation which is not preferred. This trend will be further clarified in the next section.

Figure 12 shows that the optimal charging rate for the entire Pareto set is close the maximum rate of 1C. At the first glance, this seems counterintuitive, because from the battery degradation map (shown in Figure 7) we see that the battery degradation rate is higher at higher charge rates. However, it is also evident that by increasing the charge rate we decrease the charging duration. Thus, the high-rate battery degradation process due to fast charging takes place for a shorter period of time. Hence, the resultant damage can be smaller if reducing the total battery degradation due to reducing the charging duration dominates the increase of degradation due to fast charging. The obtained optimal results indicate that this condition holds true, at least within the range of 0-1C charging, according to the employed battery model.
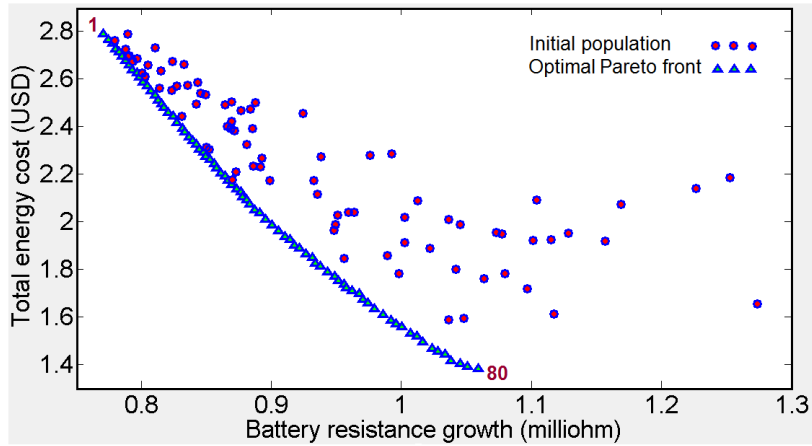
Figure 10. Optimal Pareto front for the PHEV charge pattern obtained using NSGA-II.
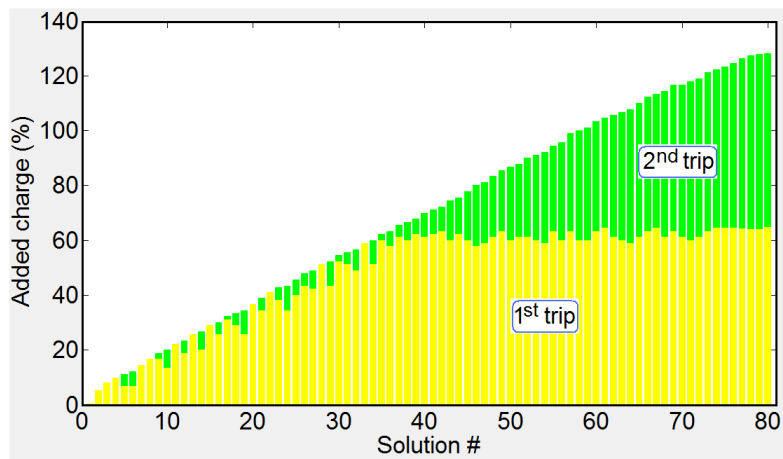


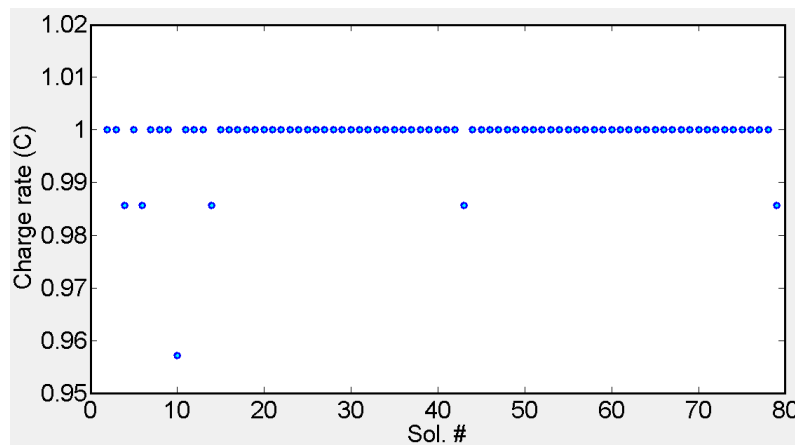Figure 11. The total amount of added charge and the portion of each trip for the optimal Pareto front solutions.



Figure 12. Charge rate distribution within the optimal Pareto front solutions.

*5.2. Sample Optimal Charge Patterns*

In this section, we present and compare the charge patterns corresponding to four sample solutions selected from the optimal Pareto front shown in Figure 10. These solutions include the charge patterns associated with least battery degradation, i.e. Sol. #1, and least energy cost, i.e. Sol. #80, as well as two middle solutions, i.e. #27 and #53, which represent different tradeoffs between the two optimization objectives. The corresponding charge patterns are plotted in Figure 13(a-d) along with the drive cycle and the electricity pricing policy.

- The first choice (Sol. #1) corresponds to the least battery degradation solution. There is no charge added to the battery, and thus, the SOC remains at the lowest limit for all time. This is essential to keep the battery degradation minimal based on the analysis provided in Sec. 3.4. The battery receives no external charge, and the PHEV operates as a conventional HEV.

- The second selected solution, i.e. Sol #27, trades off the energy cost and battery health objectives with more preference towards battery health. As depicted in Figure 13(b), a charge amount of about 50% is added to the battery before the first trip only, and the charging is delayed until before the start of the trip. The reason for this delayed charging is to avoid the unnecessary degradation due to storage at high SOCs, and the best way to achieve this is to deplete the battery soon after charging.

- Solution #53 also trades off the optimization objectives, but with more weight on energy cost. As seen from Figure 13(c), both trips include charging, with the first trip receiving full charge (65%) while the second one receiving about 30% added charge. The first charging is delayed until the first trip departure time, while the second charging is delayed until the time of transitioning to on-peak electricity pricing. Therefore, PHEV charging takes place during off-peak hours only.

- The last solution, i.e. Sol. #80, corresponds to the charge pattern that results in the least energy cost. The only difference between this solution and Sol. #53 is that the PHEV receives full charge before both trips.

The charge patterns shown in Figure 13(d) exhibit a slow increase in the input power profile, followed by a rapid drop towards the end of charging. This input power profile results from the CC-CV charging strategy. During the CC phase, battery voltage increases slightly, resulting in a commensurate increase in battery power. During the CV phase, however, the applied current drops in a controlled way to keep the voltage constant. This is the reason for the sharp drop within the last minutes of charging in Figure 13.
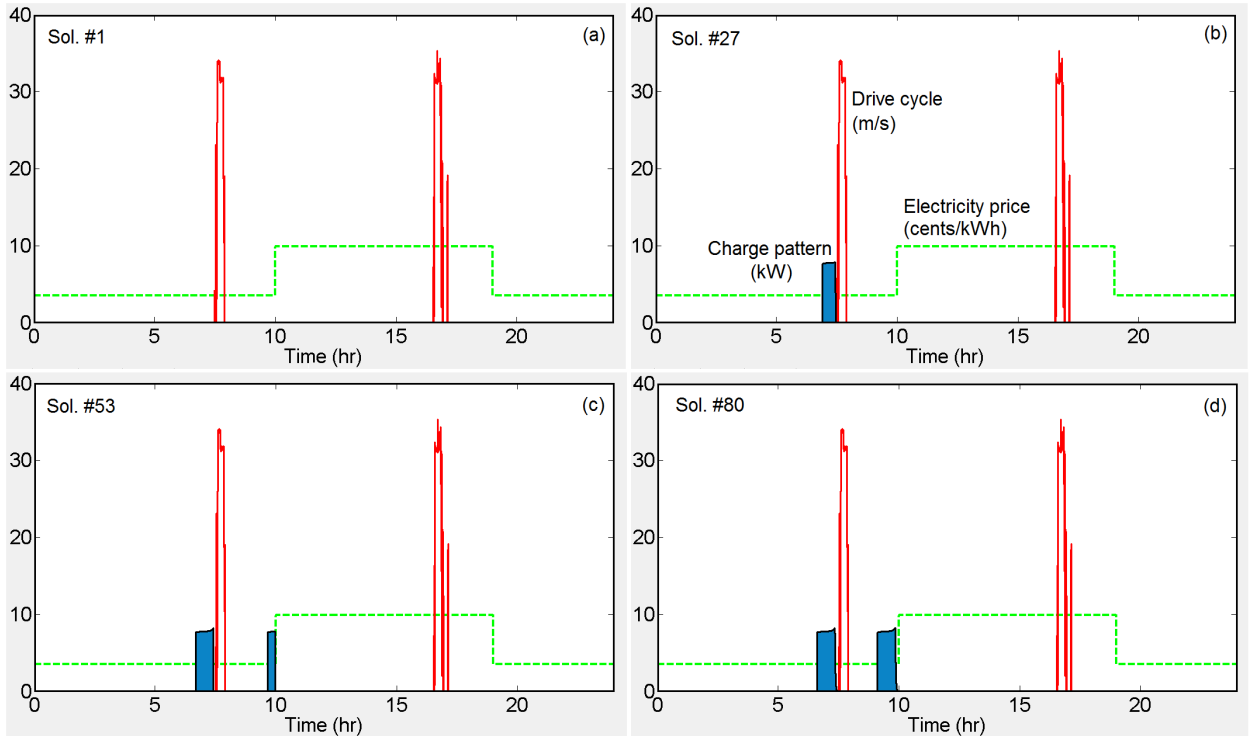


Figure 13. Four sample optimal PHEV charge patterns corresponding to: (a) Sol. #1 (least battery degradation), (b) Sol. #27, (c) Sol. #53, and (d) Sol. #80 (least energy cost).

Future work by the authors will extend the above optimization and analysis of PHEV charge patterns for different battery sizes, drive cycles, and electricity pricing policies. One key goal will be to use the charge pattern optimization approach presented in this paper to predict the aggregate load imposed by a number of PHEVs on the power grid.

## 6- Summary and Conclusions

This paper investigates the problem of optimizing PHEV charge pattern for simultaneous reduction of energy cost and battery life degradation. A PHEV model, a battery degradation model, and a multiobjective genetic algorithm are used to optimize the PHEV charge pattern for a 24-hour naturalistic drive cycle. This optimization results in the formation of a Pareto front on which the objectives are traded off optimally. Comparing different solutions from the Pareto front indicates that to effectively minimize battery degradation and energy costs, one should ideally charge a PHEV rapidly, off-peak, and shortly before the onset of road travel. These results are obtained specifically using an electrochemistry-based model of anode-side SEI growth in lithium-ion batteries, and assuming that such SEI growth is a key factor governing battery degradation and that it occurs during all phases of battery operation. The paper provides preliminary validation results for this model versus experimental data, and the methods presented in the paper are broad and generalizable to other battery degradation models as well. The paper's uniqueness stems from the fact that it optimizes PHEV charge patterns for both battery health and energy cost, for the first time.

## Acknowledgment

## References

[1]     Kempton W., Tomic J., 2005. Vehicle-to-grid power fundamentals: calculating capacity and net revenue. Journal of Power Sources, 144, 268-279.

[2]     Kempton W., Tomic J., 2005. Vehicle-to-grid power implementation: From stabilizing the grid to supporting large-scale renewable energy. Journal of Power Sources, 144, 280-294.

[3]     Marano V., Rizzoni G., 2008. Electric and economic evaluation of PHEVs and their interaction with renewable energy sources and the power grid. Proceedings of the 2008 IEEE International Conference on Vehicular Electronics and Safety, Columbus, OH.

[4]     Guille C., Gross G., 2009. A conceptual framework for the vehicle-to-grid (V2G) implementation. Energy Policy, In Press.

[5]     Hadley S., Tsvetkova A., 2008. Potential impacts of Plug-in Hybrid Electric Vehicles on regional power generation. ORNL/TM report.

[6]     Markel T., Pesaran A., 2007. PHEV energy storage and drive cycle impacts. 7th Advanced Automotive Battery Conference, Long Beach, CA.

[7]     Ichimura M., Shimomura M., Takeno K., Shirota R., Yakami J., 2005. Synergistic effect of charge/discharge cycle and storage in degradation of lithium-ion batteries for mobile phones. 27th International Conference on Telecommunications, 245-250.

[8] Jungst R. G., Nagasubramanian G., Case H. L., Liaw B. Y., Urbina A., Paez T. L., Doughty D. H., 2003. Accelerated calendar and pulse life analysis of lithium-ion cells. Journal of Power Sources, 119, 870-873.

[9] Peterson S. B., Apt J., Whitacre J. F., 2009. Lithium-ion battery cell degradation resulting from realistic vehicle, and vehicle-to-grid utilization. Journal of Power Sources (available online).

[10] Kim Y. H., Ha H. D., 1997. Design of interface circuits with electrical battery models. IEEE Transactions on Industrial Electronics, 44, 81-86.

[11] Moss P. L., Au G., Plichta E. J., Zheng J. P., 2008. An electrical circuit for modeling the dynamic response of Li-ion polymer batteries. Journal of the Electrochemical Society, 155, A986-A994.

[12] Doyle M., Fuller T. F., Newman J., 1993. Modeling of galvanostatic charge and discharge of Lithium/polymer/insertion cell. Journal of Electrochemical Society, 140, 1526-1533.

[13] Fuller T. F., Doyle M., Newman J., 1994. Simulation and optimization of the dual Lithium ion insertion cell. Journal of Electrochemical Society, 141, 1-10.

[14] Ramadass P., Haran B., Gomadam P., White R., Popov B., 2004. Development of first principles capacity fade model for Li-ion cells. Journal of Electrochemical Society, 151, 196-203.

[15] Arora P., White R., 1998. Capacity fade mechanisms and side reactions in lithium-ion batteries. Journal of Electrochemical Society, 145, 3647-3667.

[16] Deb K., Pratap A., Agarwal S., Meyarivan T., 2002. A fast and elitist multiobjective genetic algorithm: NSGA-II. IEEE Transactions on Evolutionary Computation, 40, 181-197.

[17] Moura S. J., Fathy H. K., Callaway D. S., Stein J. L., 2008. A stochastic optimal control approach for power management in plug-in hybrid electric vehicles. Proceedings of the 2008 ASME Dynamic Systems and Control Conference, Ann Arbor, MI.

[18] Moura S. J., Callaway D. S., Fathy H. K., Stein J. L., 2010. Tradeoffs between battery energy capacity and stochastic optimal power management in plug-in hybrid electric vehicles. To appear in the Journal of Power Sources.

[19] DTE Energy website, Residential Electric Rates: (http://www.dteenergy.com/residentialCustomers/billingPayment/rates/electric/resRates.html)

[20] O'Keefe M. P., Markel T., 2006. Dynamic programming applied to investigate energy management strategies for a plug-in HEV. National Renewable Energy Laboratory, Golden, CO, Report # NREL/CP-540-40376.

[21] Gong Q., Li Y., Peng Z. R., 2008. Trip-based optimal power management of plug-in hybrid electric vehicles. IEEE Transactions on Control Systems Technology, 57, 3393-3401.

[22] Wipke W. B., Cuddy M. R. and Burch S. D., 1999. ADVISOR 2.1: A user-friendly advanced powertrain simulation using a combined backward/forward approach. IEEE Transactions on Vehicular Technology, 48, 1751-1761.

[23] Santhanagopalan S., Guo Q., Ramadass P., White R., 2006. Review of models for predicting the cycling performance of Lithium ion batteries," Journal of Electrochemical Society, 156, 620-628.

[24] Plett G. L., 2004. Extended Kalman filtering for battery management systems of LiPB-based HEV battery packs: Part 1. Background. Journal of Power sources, 134, 252-261.

[25] Plett G. L., 2004. Extended Kalman filtering for battery management systems of LiPB-based HEV battery packs: Part 2. Modeling and identification. Journal of Power sources, 134, 262-276.

[26] Plett G. L., 2004. Extended Kalman filtering for battery management systems of LiPB-based HEV battery packs: Part 3. State and parameter estimation. Journal of Power sources, 134, 277-292.

[27] Verbrugge M., 2007. Adaptive, multi-parameter battery state estimator with optimized time-weighting factors. Journal of Applied Electrochemistry, 37, 605-616.

[28] Cai L., White R., 2009. Reduction of model order based on proper orthogonal decomposition for lithium-ion battery simulations. Journal of the Electrochemical Society, 156, A154-A161.

[29] Ramadesigan V., Boovaragavan V., Arabandi M., Chen K., Tsukamoto H., Braatz R. D., Subramanian V. R., 2009. Parameter estimation and capacity fade analysis of lithium-Ion batteries using first-principles-based efficient reformulated models. ECS Transactions, 19, 11-19.

[30] Subramanian V. R., Boovaragavan V., Diwakar V., 2007. Toward real-time simulation of physics based lithium ion battery models. Electrochemical and Solid-State Letters, 10, A255-A260.

[31] Forman J., Bashash S., Fathy H. K., Stein J. L., 2010. Model reduction of a degrading electrochemical Li-ion battery model via constraint linearization and Padé approximation. Submitted to the Journal of Electrochemical Society.

[32] A123 Systems website: www.a123systems.com.

[33] A123 Systems, 2007. Development of battery packs for space applications. NASA Aerospace Battery Workshop, Huntsville, AL.

**Figure Captions**

Figure 1. PHEV model components, supervisory controller, and signal flow. Note that the signal flow forms a state feedback control architecture.

Figure 2. A sample suburban naturalistic drive cycle with two half trips, one in the morning and one in the afternoon (vehicle velocity is zero during the rest of the day).

Figure 3. Energy costs versus initial battery SOC for the optimal power management strategy with two different battery sizes: an 8 kWh (top) and a 16 kWh battery (bottom).

Figure 4. Custom-built experimental battery test system used for parameter identification and validation of the high-fidelity battery model.

Figure 5. Experimental battery parameter identification results: (a) Applied current profile, and (b) Experimental and model voltage responses.

Figures 6. Comparison between the battery model and the experimental manufacturer data in (a) CC-CV cycling and (b) full-charge storage modes.

Figure 7.  Battery degradation map.

Figure 8. Battery degradation response in energy storage.

Figure 9. Schematic diagram of the PHEV charge pattern optimization process.

Figure 10. Optimal Pareto front for the PHEV charge pattern obtained using NSGA-II.

Figure 11. The total amount of added charge and the portion of each trip for the optimal Pareto front solutions.

Figure 12. Charge rate distribution within the optimal Pareto front solutions.

Figure 13. Four sample optimal PHEV charge patterns corresponding to: (a) Sol. #1 (least battery degradation), (b) Sol. #27, (c) Sol. #53, and (d) Sol. #80 (least energy cost).